LA-UR-20-20210 (Accepted Manuscript)

Shock initiation of the HMX-based explosive PBX 9012: Experiments, uncertainty analysis, and unreacted equation-of-state

Burns, Malcolm John
Chiquete, Carlos

To be published in: Journal of Applied Physics

DOI to publisher's version: 10.1063/1.5144686

Permalink to record: http://permalink.lanl.gov/object/view?what=info:lanl-repo/lareport/LA-UR-20-20210

Shock initiation of the HMX-based explosive PBX 9012: experiments, uncertainty analysis and unreacted equation-of-state

M.J. Burns[1, a)] and C. Chiquete[1]
Los Alamos National Laboratory, P.O. Box 1663, Los Alamos, NM 87545, USA.

(Dated: 11 May 2020)

Shock initiation experiments have been carried out on the polymer-bonded explosive PBX 9012 (nominally 90% HMX, 10% Viton A by weight) in order to provide calibration data for the explosive's unreacted equation-of-state (EOS) and shock-to-detonation transition for reactive burn rate calibration. The input pressures covered the range 2.00 to 4.43 GPa. This provided run-to-detonation depths ranging from >22.3 mm for the lowest pressure shot to 4.91 mm at the highest pressure. The relative shock sensitivity of PBX 9012 is compared to other HMX-explosives in terms of the Pop-plot, showing that the studied explosive is more sensitive than other similar HMX-based counterparts (with notable exceptions). The uncertainty in the shock velocity determinations from the shock tracker measurements are also investigated, yielding new uncertainty measures in the generated Hugoniot data and run-to-detonation coordinates. Finally, the unreacted equation-of-state is determined using a linear $U_s - u_p$ Mie-Grüneisen relation and the Davis reactants EOS analytical form, the latter being more suited for reactive burn modeling.

I. INTRODUCTION

In this work we collate the results of a series of five shock initiation experiments on the polymer-bonded explosive PBX 9012, nominally composed of 90% octahydro-1, 3, 5, 7-tetranitro-1, 3, 5, 7-tetrazine (HMX) explosive and 10% vinylidene-hexafluoropropene copolymer (Viton A) binder by weight and nominal density of 1.845 g/cm^3. This particular formulation has received renewed interest as a component in initiation train engineering designs. Note that the exact same formulation had been originally studied in the late 1960's, then identified as LX-07[1]. The ultimate aim of this current work is to build up a calibrated reactive burn model for PBX 9012 to aid design work and in this paper we report both on our experimental and initial modeling efforts.

TABLE I: Selected HMX-based explosive composition (by wt. %) and nominal densities. Descriptions of non-HMX components are summarized in Table II.

Explosive	Composition	Density (g/cm^3)
LX-04[2]	HMX 85%, Viton A 15%	1.845
LX-07[1]	HMX 90%, Viton A 10%	1.860
PBX 9012	HMX 90%, Viton A 10%	1.845
PBX 9404[2]	HMX 94%, NC 3%, CEF 3%	1.844
LX-10[1]	HMX 95%, Viton A 5%	1.860
PBX 9501[2]	HMX 95%, Estane 2.5%, BDNPA/BDNPF 2.5%	1.830

The explosive molecule used in PBX 9012 and LX-07, HMX, is also the primary energetic component of other previously studied PBXs including the LX-04, LX-10, PBX 9501 and PBX 9404 (see Table I for a relevant selection). These explosives differ only in the weight percentage of HMX and chosen type of (mechanically) stabilizing binder. As mentioned,

TABLE II: Description of minor components for HMX-based explosives.

Component	Description
Viton A	vinylidene hexafluoropropene dipolymer
CEF	tris-beta chloroethylphosphate
NC	nitrocellulose
Estane	polyester urethane random copolymer
BDNPA/BDNPF	eutectic mixture of bis(2,2-dinitropropyl)acetal and bis(2,2-dinitropropyl)formal

LX-07 shares the same nominal components and weight percentage composition as modern PBX 9012 but differs significantly in the nominal initial density (Green et al[1] list this as 1.86 g/cm^3). It is reasonably clear that increasing HMX content increases performance, i.e. detonation velocity and post-detonation pressure. On the other hand, the specific binder and explosive grain size distribution has a less intuitive effect on the shock initiation behavior leading to significant differences in this sense, even when these have essentially equivalent HMX content. This is typically explained via the observation that the porosity or void structure in a given PBX matrix is known to be a major influence on the sensitivity of the explosive to shock-loading – a likely consequence of the hot-spot mechanism for explosive ignition where it is thought that collapsing voids precipitate localized high-temperature zones which ultimately serve to ignite the surrounding explosive grains. In practice, the pressing density of the explosive is a controlling quantity in this process as it directly influences the void percentage (usually of a few percent). This is of interest here as the initial HE density of PBX 9012 differs by 0.015 g/cm^3 from the nominal LX-07 density. For the related explosive PBX 9501, Gustavsen et al[3] found that density differences of only 0.004 and 0.007 g/cm^3 were sufficient to produce significant changes in the initiation behavior. These experimental observations underlie our current need to specifically characterize PBX 9012 under shock initiation.

a)Electronic mail: mjburns@lanl.gov

In its possible use in explosive initiation trains, characterization of the initial transient shock wave propagation for PBX 9012 in the growth phase of reaction under shock loading is specially important. Historically, one-dimensional shock initiation experiments have been used to produce data for model comparison and calibration. In particular, the wedge test experiment has been commonly used to track the progress of planar shocks as they break out at the streak-camera-imaged plane (inclined to the front propagation direction) after initiation by the impact of a projectile or flyer at a controlled velocity. Different projectile velocities can be used to span a range of stimuli into the explosive, generally showing how the run-to-detonation distance decreases with higher impact velocity and therefore higher input pressure. More recently, with the advent of embedded gauges[4] such as those used in this paper, we have gained access into the reaction zone profile of the particle velocity (u_p) which represents a richer data set for model comparison (which has previously been limited to the shock track behavior revealed by the wedge test).

Shock initiation experiments provide significant insight into an explosive's unreacted Hugoniot and equation-of-state (EoS) and the growth of reaction under shock loading. These are essential components of reactive flow modeling of explosives at the continuum level[5,6], i.e. where tractable simulations of engineering-scale, multi-dimensional HE geometries are possible. Given the structural complexity of solid explosive molecules and the polymeric binders that are typically used, reliable first-principles determinations of these constitutive models are still beyond our current capability. Therefore, to ensure a reliable prediction, we still require experimental observations such as those undertaken here to parameterize HE models as new explosive formulations are generated or previous formulations are revisited (as is the case for PBX 9012).

In this work, we first describe the setup of our experiments and present selected experimental results. Specifically, the reactive growth behind the shock front will be presented in terms of the particle velocity wave profiles. The relative shock sensitivity of PBX 9012 will be presented in the form of the Pop-plot[7]. A new uncertainty analysis of the previously-established procedure that determines the shock velocity (U_S) needed to characterize the shock Hugoniot and run-to-detonation coordinates is also given. Finally, in terms of model development, the unreacted EoS will be presented both in terms of the standard linear $U_S - u_p$ relation and also in the form of a Davis reactants analytical form[6,8].

II. EXPERIMENTAL DETAILS

The samples used have been machined from 2" die-pressed parts, with the shock running in the pressing direction. The nominal density of the PBX 9012 is 1.845(1) g/cm^3. As a side note, the uncertainties of measurement presented in this paper follow the Guide to the Expression of Uncertainty in Measurement (GUM)[9]. As such the notation 1.845(1) g/cm^3 is equivalent to 1.845 $\pm$ 0.001 g/cm^3. In addition, throughout our paper, when we cite the standard uncertainty, we are referring the non-expanded uncertainty. Compositional analysis[10] of the explosive samples (material lot 1733927401) showed only a slight variation from the nominal or intended composition during pressing, i.e. 90.20(15)% HMX and 9.80(15)% Viton A binder by weight. The setup of our experiments follows the electromagnetic particle velocity (EMV) methodology[4] which is designed to produce in situ measurements of the reaction zone in the shocked explosive. Both single and two-stage gas guns were used, with bore diameters of 76 and 50 mm respectively, leading to maximum one-dimensional shock loading depths of 36 and 25 mm. The gas guns were used to launch two types of impactors in the velocity range of 0.46 to 1.56 km/s: Kel-F (a 3/1 copolymer of chloro-trifluoroethylene and vynylidene-fluoride) and sapphire. These impact targets which typically consist of a split cylindrical wedge which were embedded with the EMV gauges.

TABLE III: Linear Hugoniot parameters used in the experiment design phase for the impactor and target materials.

Material	C_0 (mm/μs)	S	Density (g/cm^3)
Sapphire (c-cut)	11.19	1.00	3.985
Kel-F81	1.836	1.878	2.12
PBX 9012 (estimate)	1.77	2.61	1.92

Figure 1 shows the embedded gauges with the individual gauge elements and the three tracker gauges annotated. The gauge package consists of nine particle velocity gauges nested one inside the other with the active element of the gauge being the horizontal part of the gauge. The gauge consists of thin (≈ 5 μm) aluminum elements sandwiched between insulating sheets of Fluorinated Ethylene Propylene (FEP) Teflon. When the shock drives the active part of the gauge (at particle velocity u_p) through an applied magnetic field (B) it produces the net voltage (V) according to

$$V = BLu_p, \tag{1}$$

where the length (L) of the active elements range from ≈ 7 to 15 mm. Typically these gauges are placed at an angle of 30°, resulting in a depth spacing of ≈ 0.8 mm in the direction of the shock and covering a depth ranging from around 1 to 9.5 mm. Surrounding the nested particle velocity gauges are the three shock tracker gauges. These ladder-like structures provide a change in the polarity of the voltage signal as the shock transits between each rung in the ladder. This provides 117 individual measurements of the shock position as a function of time.

The gauges are glued onto the bottom wedge with careful alignment to the impact plane. The top wedge is then glued in place with a glue bond thickness in the region of five microns. The complete gauge layer is typically less than fifty microns. The front surface of the target is machined flat and a single element EMV *stirrup* (ST) gauge is glued onto the impact surface, see Figure 1.

The Hugoniot linear $U_S - u_p$ fits used in the design phase of this work for both projectiles (Kel-F[11,12] and sapphire[13])

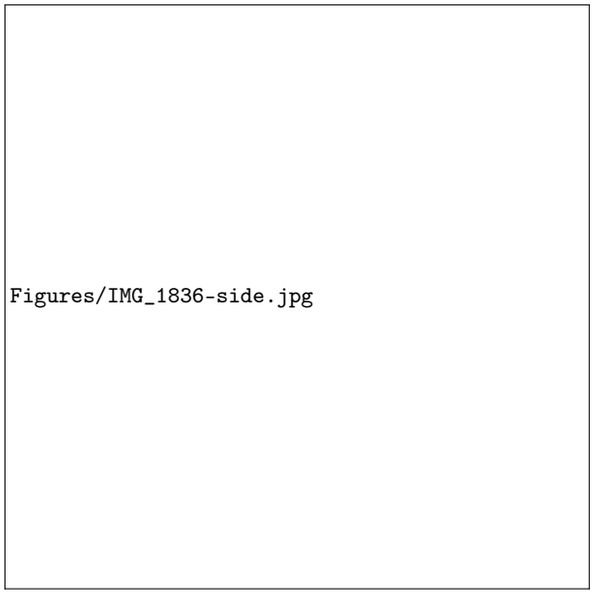

FIG. 1: A) Photo of EMV gauge detailing the nine gauges (G1 to G9), the left tracker (LT), right tracker (RT) and the center tracker (CT). B) Photo of experimental setup showing both wedges, the stirrup (ST) gauge on the impact plane and the embedded electromagnetic particle velocity (EMV) gauge.

and target[14] are presented in Table III. It should be stressed that the PBX 9012 Hugoniot was estimated using the Hugoniots for LX-10 (95% HMX) and LX-04 (85% HMX) which were used to generate a composite Hugoniot for LX-07 (compositional twin to PBX 9012). These values are therefore not the measured shock Hugoniot for LX-07 or PBX 9012. Note that there has not been a comparative study of the particle size distribution or fabrication methodologies between LX-07 and PBX 9012 but LX-07 was nevertheless considered a suitable proxy for experimental design purposes. The results from each experiment were analyzed before the next experiment was fired, in order to adjust the input shock pressures to our desired range.

III. RESULTS

The input conditions of the five experiments are presented in Table IV. These conditions take the form of the shock pressure (P), particle velocity (u_p) and shock velocity (U_S) along with the run-to-detonation coordinates in depth (X_D) and time (T_D) from the impact surface (the process to define these is detailed in § III D). The input shock pressure (P) is obtained using

$$P = \rho_0 U_S u_p, \tag{2}$$

where the measured input particle velocity (u_p) was taken from the stirrup gauge data, the density (ρ_0) measured by immersion during the build process and the shock velocity (U_S) taken from the velocity time curve as seen in Figure 3 at the intersection of the y-axis. The input pressures were chosen such that the run-to-detonation distances spanned the depth range of the gauges. The input shock pressures ranged from 2.00 to 4.43 GPa, resulting in turnover to detonation depths from $\geq$ 22.3 to 4.91 mm from the impact plane. The uncertainties shown in Table IV are a combination of experimental measurements during the build and a simulated approach to determining the uncertainties in the extraction of the detonation coordinates from the fitted acceleration function; the latter is described in detail in § III E.

A. Wave-profiles

Figure 2 shows the particle velocity histories obtained from the nine embedded gauges and the stirrup gauge in test 1s-1673. The input pressure for this experiment was 3.97 GPa, leading to a corresponding input particle velocity of 0.614 mm/μs. As the shock progresses deeper into the explosive (gauge depths are presented in the legend) the measured particle velocity can be seen to grow, both at and behind the shock front. This is characteristic of reaction growth in a heterogeneous explosive with the likely mechanism being dominated by chemical processes radiating from critical hot spot sites. As the reaction rate increases we see a turnover from a reaction induced shock growth to a self-sustaining detonation wave. This can be seen as the triangular shaped profile at a depth of 5.36 mm. We see a steep change in particle velocity at the detonation front, nominally to the CJ conditions as the gauges do not have the temporal resolution to resolve the von Neumann spike, followed by the immediate Taylor decay.

B. Position-Time ($X-T$) trajectories

The shock tracker data from the experiment 1s-1673 is presented in Figure 2 (b). As the shock wave progresses through the explosive it imparts movement as it sweeps past each rung of the ladder, allowing a measurement coordinate at each of these sites. The coordinates are measured in the position-time ($X-T$) plane with the position being determined by careful metrology of the target and gauge during the build process and the time coordinate being measured directly from the raw tracker data. As the shock velocity increases and turns over to detonation the time between oscillations lessens. This can be seen in the raw tracker data, and is also evident as a change in gradient of the $X-T$ data as shown in Figure 2 (b) – consistent with the wave profile change in Figure 2(a). These trends are represented in the following acceleration function[15],

$$a(U_S) = a_m \left(\frac{D_{max} - U_S}{D_{max} - U_m} \right) \exp\left(\frac{U_S - U_m}{D_{max} - U_m} \right), \tag{3}$$

where $a = dU_S/dT = d^2X/dT^2$ is the shock acceleration, a_m is the maximum shock acceleration, D_{max} is the saturated or maximum detonation velocity, U_S is the shock velocity and U_m is the shock velocity at maximum acceleration. This fitting function mathematically encodes the constant velocity of

TABLE IV: Particulars for the five PBX-9012 experiments including input conditions and detonation coordinates. For shots using the single stage gas gun, the shot number is annotated with "1s" and the two-stage gas gun shot with "2s". * The data for shot 1s-1675 show that it reached a shock velocity around 93% of the expected detonation velocity. As such the values quoted are the minimum likely values based on the deepest measured shock arrival time.

Shot No.	Impactor	Proj. Vel. (km/s)	ρ_0(target) (g/cm^3)	P (GPa)	u_P (mm/μs)	U_S (mm/μs)	X_d (mm)	T_d (μs)
2s-1101	Kel-F	1.555(1)	1.845(1)	4.43(7)	0.716(9)	3.35(3)	4.91(10)	0.95(2)
1s-1673	Sapphire	0.708(1)	1.846(1)	3.97(7)	0.614(10)	3.50(2)	6.21(4)	1.47(1)
1s-1674	Sapphire	0.560(1)	1.845(1)	2.32(4)	0.460 (6)	2.73(2)	12.11(8)	3.03(1)
1s-1675*	Sapphire	0.456(1)	1.844(1)	1.86(3)	0.377(6)	2.68(1)	>22.30	>6.05
1s-1684	Sapphire	0.605(1)	1.844(1)	3.10(4)	0.513(6)	3.28(2)	8.76(5)	2.30(1)

detonation at the end of the experimental run, i.e. $a \to 0$ as $U_S \to D_{max}$ and an inflection point at $U_S = U_m$. The specific form used by Hill and Gustavsen[15] is motivated by a near-Chapman-Jouguet limit asymptotic relation between the (planar) shock velocity and its acceleration, derived in the broader context of multidimensional detonation propagation[16]. To represent the velocity at any time (including the gauge arrival times), the shock tracker path and velocity is calculated from the acceleration function through solution of the ordinary differential equation system,

$$\begin{aligned} &dX/dT = U_S,\ d^2U_S/dt^2 = a(U_S), \\ &X(T=0) = X_0, U_S(T=0) = U_0, \end{aligned} \tag{4}$$

where X_0 and U_0 are the initial condition parameters. Analytic solutions to the initial value problem defined in (4) can be found and require evaluations of integral functions and their inverses. Alternatively, one can also simply integrate the initial value problem instead. Integration of (4), given a candidate set of initial parameters a_m, U_m, D_{max}, X_0 and U_0, produces a direct comparison to the shock tracker data, which is essentially spatial and temporal coordinates for the shock position. The fit quality of the model calculation is maximized by a least-squares error minimization approach, producing the optimal set of parameters.

Though uncertainties in the projectile velocity or signal rise times have been previously incorporated into Hugoniot data determinations[17], less is known about the uncertainty generated in the determination of the shock velocity that results from the shock track fitting procedure. Clearly, there is some level of experimental uncertainty in the shock track positions and times and this can be propagated through the shock track fitting procedure. This is explored here in § III E for the first time, to our knowledge.

C. Shock Hugoniot

One of the benefits of having ten gauge locations embedded within the target is that we can gain up to ten data points on the unreacted Hugoniot from each experiment. This is possible due to the reaction fraction at the shock front being zero. For each embedded gauge location, the particle velocity at the shock fronts can be measured. However, in practice, due to inherent sampling resolution issues in the experiments, extraction of post-shock particle velocities for cases near or at detonation is avoided. The uncertainty in this measurement is taken as the local standard deviation where particle velocity is being extracted from the wave-profile data. If there is significant overshoot, likely caused by ringing in the glue layer, the uncertainty is increased to half the height of the overshoot. The location of the measurement is taken from the wave-profiles and is the intersection of a straight line fit to the shock portion of the data and a quadratic fit to the subsequent reactive growth immediately following the shock. The time at this intersection point is then used to extract the shock velocity from the time-derivative of the $X-T$ functional fit obtained in § III B, shown in Figure 3 specifically for test 1s-1673.

The shock velocity data can then be presented as a function of particle velocity as shown in Figure 4. The shock and particle velocities used to develop the linear Hugoniot for PBX 9012 are presented both in Table V and Figure 4. The Hugoniot is described by,

$$U_S = 1.99(6) + 2.80(15)u_p. \tag{5}$$

where the intercept is constrained to an experimental measurement of the sound speed in the explosive. Note that a more complex EoS, suitable for application in reactive burn models, is derived from this data in § IV. The sound speed was specifically measured[10] using the time-of-flight method. An acoustic pulse was applied to one side of the sample using a piezoelectric transducer and was measured on the other side of the sample using an identical transducer. The times of the input pulse generation and transmitted pulse detection were measured and divided by the sample thickness to give the acoustic velocity. Both longitudinal wave (P-wave) and shear wave (S-wave) transducers were used. The transducers were specifically Panametrics, 1-inch diameter piezoelectric transducers, models V102 and V152 for P-wave and S-wave, respectively. The longitudinal (V_l) and shear (V_s) velocities were combined using

$$V_B = \sqrt{V_l^2 - 4V_s^2/3}, \tag{6}$$

to obtain the bulk sound velocity (V_B).

(a)

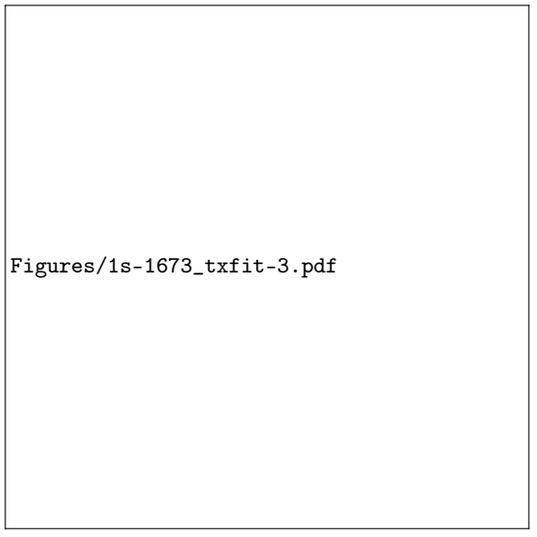

(b)

FIG. 2: a) Particle velocity wave profiles for shot 1s-1673, input pressure 3.97 GPa. b) $X-T$ data and fit plot for shot 1s-1673, extracted from the gauge metrology and the raw tracker data. The cyan data points in the inset are the fit residuals. The black vertical dashed line represents the run-to-detonation time in both plots and the horizontal line in b) is the run-to-detonation distance. The green dotted lines are the gauge trigger times in the shock track plot (b).

D. Pop-plot

The Pop-plot[7] represents a relative ordering in shock sensitivity of an explosive subject to a planar input pressure wave. When the run distance to detonation is plotted as a function of input pressure and the data is plotted on a log-log plot, the data tend to lie on a straight line for any given explosive, or indeed any subset of explosive characteristics, such as temperature or density. As this line trends towards the origin an increase in shock sensitivity can be inferred.

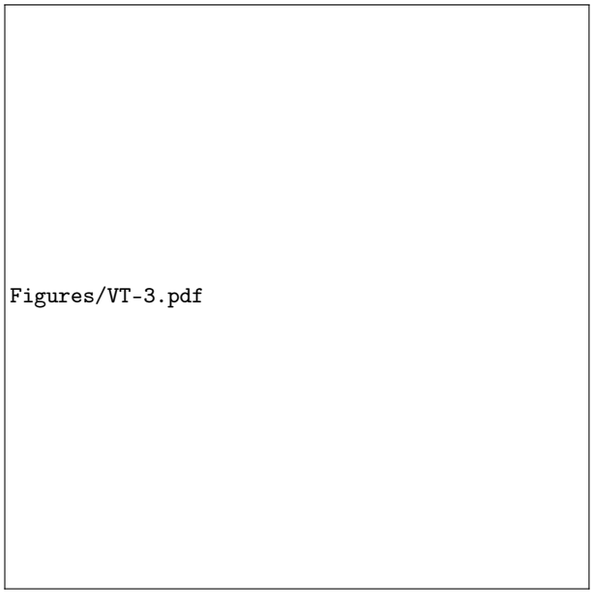

FIG. 3: Shock velocity vs. time curve derived from the fit to the $X-T$ data for shot 1s-1673. Vertical and horizontal dashed lines represent the detonation time and velocity threshold (obtained from the condition that $U_S = 0.95\ D_{max}$). The solid circles represent the gauge arrival times for this shot. The inset shows the acceleration function obtained from the fit for the relevant time range prior to detonation.

TABLE V: Shock Hugoniot data as $U_S - u_p$ pairs with included experimental uncertainties. Derivation of uncertainty values for the shock velocities appear in § III E.

u_p (mm/μs)	U_S (mm/μs)	u_p (mm/μs)	U_S (mm/μs)
0.614(10)	3.503(24)	0.456(90)	3.645(10)
0.566(15)	3.773(23)	0.540(66)	3.780(10)
0.601(16)	3.919(23)	0.618(25)	3.936(11)
0.696(22)	4.176(23)	0.750(30)	4.110(11)
0.940(19)	4.567(26)	0.716(9)	3.349(34)
0.460(6)	2.728(38)	0.855(40)	4.371(50)
0.552(10)	3.830(48)	0.933(40)	5.086(73)
0.713(30)	4.287(61)	1.401(40)	6.095(118)
0.923(27)	4.622(97)	0.513(6)	3.281(17)
1.333(50)	4.976(152)	0.508(30)	3.374(16)
0.377(6)	2.680(15)	0.493(30)	3.442(16)
0.421(10)	3.031(10)	0.525(40)	3.531(16)
0.416(12)	3.162(9)	0.527(30)	3.647(15)
0.397(26)	3.327(9)	0.555(40)	3.783(15)
0.398(19)	3.416(9)	0.591(100)	3.972(14)
0.432(32)	3.523(9)	1.174(40)	4.915(35)

The run-to-detonation distance is obtained following Hill et al[15]. Specifically, the detonation coordinates are taken from the shock track fit function at a velocity that is 95% of the final fitted maximum velocity. The coordinates measured for shot 1s-1673 as presented in Figure 2(b) and Figure 3 are X_D

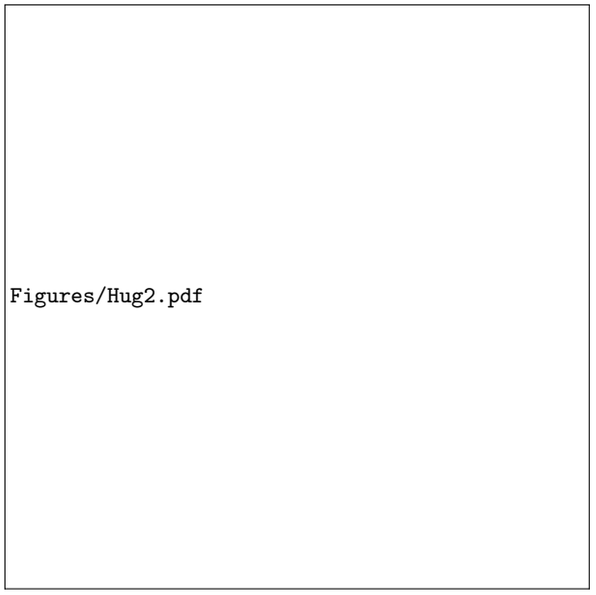

(a)

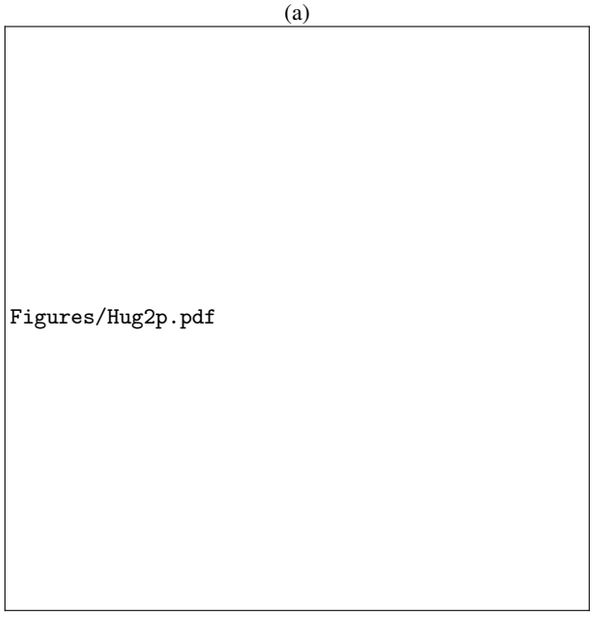

(b)

FIG. 4: Shock Hugoniot, in the a) U_S - u_p and b) $p-v$ planes, with dotted line representing the linear $U_S - U_p$ relation. Note, the sound speed measurement is represented by the data point at the intersection of the Y-axis on the U_S - u_p plot, with a value of 1.99(6) mm/μs.

= 6.21 mm and T_D = 1.47 μs. The complete list of detonation coordinates for this shot series are presented in Table IV.

Figure 5 displays the measured data for this batch of PBX 9012 and historical data obtained by Green et al[1] for LX-07 and LX-10 is also included (along with trend lines determined from the experiments). Empirical trend lines for PBX 9501[3] and 9404[18] are also included. The compositions for each of these cited explosives is compared in Table I. The dashed blue line in Figure 5 is a fit to the Pop-plot data for PBX 9012 and

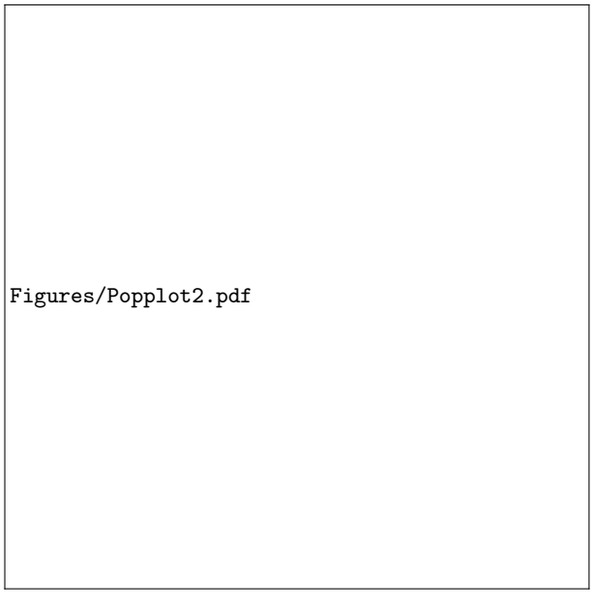

FIG. 5: Pop-plot data with error bars and trend line for PBX-9012, along with data and trend lines for selected, HMX-based explosives.

is well-described by the linear trend,

$$\log_{10}(X_D) = 1.73(7) - 1.60(15)\log_{10}(P). \quad (7)$$

The result indicates that PBX 9012 is significantly more sensitive that other previously characterized HMX-based explosives like PBX 9501 and LX-07. The higher porosity value for PBX 9012 helps explain this finding at least relative to the identically-composed LX-07, given that the theoretical maximum density for the common composition is 1.892 g/cm^3 according to Dobratz and Crawford[18]. Therefore, the porosity or void percentage for PBX 9012 was 2.5% while for LX-07 this measure was 1.7% (using a nominal density of 1.86 g/cm^3 as in Green et al[1]). Figure 5 also shows LX-10 and PBX 9404 are more sensitive than PBX 9012, at least for some range of input pressures, as determined from the empirical fits.

E. Shock velocity uncertainty

1. *Setup for analysis*

As described previously, the conventional process to determine the shock velocity from experiment is through an empirical curve fit to the shock tracker spatial position and time-of-arrival data[15]. A derivative of the shock position function then produces an estimate of the shock wave velocity for any point during the experiment. Given relevant gauge position arrival times, the shock velocity is evaluated using the differentiated fit function to produce the $U_S - u_p$ Hugoniot data. Additionally, the run-to-detonation distance is determined by defining a velocity threshold (typically, some high percentage

of the maximum shock velocity) using this function to determine the point in time and space where this occurs. Given its centrality in processing the experiments into usable data for EoS and reactive flow model development, we undertook a sensitivity analysis of this fitting process to experimental measures of the shock tracker data uncertainty in the shock spatial position and time of arrival. The approach we adopt here to do this is to produce a large set of randomly perturbed shock tracker data sets (using the experimental uncertainties in both shock position and timing) and subsequently generate a series of fitted curves to the perturbed data. With these fit variants in hand, we can then analyze the variability of the shock velocity evaluation at any time or position and additionally, of any other derived quantity such as the detonation coordinates.

Here, we focus on the sensitivity to uncertainties in the originating experimental data set itself, specifically to uncertainty in the shock tracker spatial position and timing, denoted as σ_X and σ_T, respectively. The rise time for both the shock tracker signals, and the wave profile shock arrival, were used to dimension the time-of-arrival uncertainty σ_T. The main contribution to this rise time is experimental tilt, both during the build (gauge placement) and the alignment of the target relative to the impactor. The measurement precision of gauge positions was used to estimate σ_X. To quantify the uncertainty on our shock velocity measurements, we use these experimental error measures to produce a sequence of perturbed shock tracker data points (enumerated by i), i.e. $X_i \to \tilde{X}_i, T_i \to \tilde{T}_i$, where $\tilde{X}_i$ and $\tilde{T}_i$ are now random samples from a normal or Gaussian distribution function (φ) centered at the unperturbed experimental value of each quantity,

$$\varphi(y, y_i, \sigma_y) = \frac{1}{\sqrt{2\pi\sigma_y^2}} \exp\left(-\frac{(y-y_i)^2}{2\sigma_y^2}\right). \tag{8}$$

We use the experimental standard uncertainty as the standard deviation in the Gaussian source distributions from which we repeatedly draw the randomized, perturbed analogues of the original data.

The distribution of these perturbed points can be seen in Figure 6 for shot 2s-1101 (with $\sigma_T = 0.012$ μs and $\sigma_X = 0.018$ mm), where a large accumulation of perturbed points can be seen along with the raw, unperturbed data. In total, 1000 shock tracker data variants were produced and analyzed for each shot. The convergence of fitted standard deviations from this accumulation of data tended to occur at about 500 iterates, we therefore have doubled this minimum value to ensure converged results.

2. Results

Fits were then produced from each individual set of perturbed $X-T$ data, where each element of each shot's tracker data set is perturbed independently. All of these fit variants are compared to the data in Figure 6 (in red lines) for shot 2s-1101. Additionally, the mean and standard deviation of the accumulated fit variants appear in Table VI. The standard deviations in each parameter encode the variability in the found

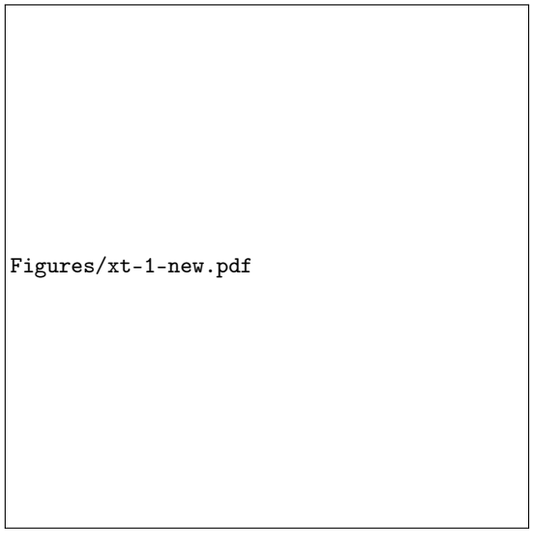

FIG. 6: The raw unperturbed data (in yellow points) and perturbed shock tracker data for shot 2s-1101. Many sets of perturbed shock tracker points are plotted (in blue points). The many fit variants associated with the perturbed shock data sets are also plotted in red lines. A zoom-in (demarked by gray rectangle) near the turnover to detonation is shown in the inset.

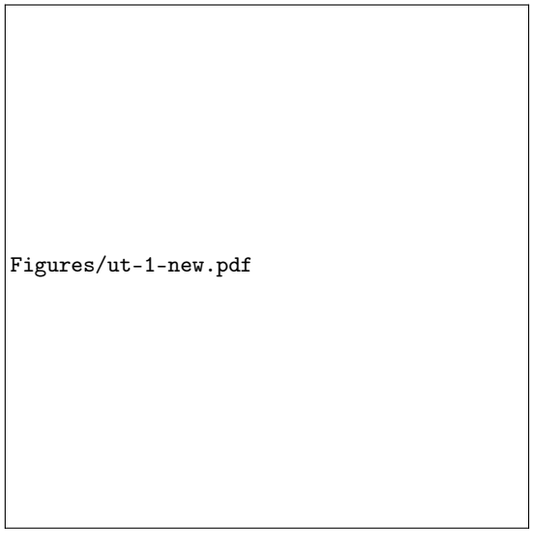

FIG. 7: The associated velocity vs T dependence from the various perturbed variants and also the baseline fit to the unperturbed data for shot 2s-1101. A zoom-in (demarked by gray rectangle) near the inflection point in the shock velocity (maximum wave acceleration) is given in the inset.

fits shown in Figure 6. Figure 7 shows the corresponding evaluations of the shock velocity variation in time. It is apparent that the uncertainty markedly increases as the point of maximum acceleration is approached, decreasing thereafter when the wave approaches a constant velocity. Given this large number of curves, the shock velocity can be evaluated at the

TABLE VI: Mean and standard deviation of the shock tracker fit parameter variants produced for shot 2s-1101.

Parameter	Mean	Std. deviation	Unit
X_0	-0.010	0.042	mm
U_0	3.32	0.03	mm/μs
a_m	10.930	0.004	mm/μs^2
U_m	7.55	0.04	mm/μs
D_{max}	8.97	0.06	mm/μs

relevant gauge times to build a distribution of the perturbed shock velocity. These distributions can then, in turn, be fitted to a normal Gaussian distribution themselves and the standard deviation (or associated standard uncertainty for our purposes) can then be determined. This is shown for two gauge times for shot 2s-1101 in Figure 8. To reiterate, Note that the distribution standard deviations tended to converge between 500-1000 iterates. This process was repeated for all shots and all the relevant gauge times – to produce the set of values previously given in Table V and plotted in Figures 4 & 11. The specific uncertainties used to produce the perturbed shock paths and associated shock velocity uncertainty measures are given in Table VII for all the shots.

TABLE VII: Spatial (σ_X) and temporal (σ_T) standard deviations used in our sensitivity calculations, with listing in terms of descending input pressure.

Shot	P (GPa)	σ_X (mm)	σ_T (μs)
2s-1101	4.43	0.018	0.012
1s-1673	3.97	0.009	0.007
1s-1684	3.10	0.010	0.006
1s-1674	2.32	0.028	0.030
1s-1675	1.86	0.009	0.010

Figure 9 shows the variation of the shock velocity standard deviation (in absolute and relative terms) for all shots, and for all times in the relevant range for each experiment, not just at the relevant gauge times. According to these results, the point of maximum uncertainty is more or less coincident with the point of maximum acceleration of the baseline shock track fit (denoted by the open circles in Figure 9). If the gauge locations were to be placed near the maximum acceleration point in the wave evolution, the associated uncertainty would also be maximized (to values as high as 500 m/s or between 4–9% of baseline shock velocity values across the shot series). This of course can't be known a priori, but the potential exists to generate very high uncertainties and the present data set shows that the point of maximum uncertainty is approached by the gauge placements in widely varying degrees (see solid circles in Figure 9). It should be said however that the time period in the wave propagation where the maximum uncertainty is achieved is generally narrow and it is unlikely that gauges placed near the transition point to detonation would be used to estimate the post shock particle velocity necessary to generate Hugoniot data (due to the decreased accuracy in capturing near-detonation particle velocities). Note that the

(a)

(b)

FIG. 8: Distributions of evaluated shock velocity at two relevant times (0.533 μs (a) and 0.690 μs) (b) in the shock wave propagation for shot 2s-1101.

presently-calculated shock velocity uncertainties are consistent with an estimate given by Gustavsen et al[19] who reasoned that wave tilt (as manifested through increased scatter in the measured $X-T$ trajectories and increased uncertainty in signal rise times) could produce apparent uncertainties of around $\pm$4.5% in the shock velocity (assuming 10 milliradians of tilt for a shock velocity of 6 mm/μs). This representative calculation did not involve analysis of the specific shock track data as we performed here.

For the shock Hugoniot data, which is essential in determining the unreacted EoS, the uncertainty measures derived here are generally smaller than the data spread in U_S seen in Figure 4. Since the any derived EoS model will clearly not fit all the data points to within the determined standard uncertainty

in each measurement (as can be seen for the linear $U_s - U_p$ relation and the Davis reactants fit detailed in § IV), we expect that the dominant factor contributing to model uncertainty in this case is the relatively large spread in the data as a whole, rather than the uncertainty for a particular point. That said, the analysis developed here indicates that the higher shock velocity values, which occur later in the acceleration phase, tend to be more uncertain, so the associated extrapolation to the von Neumann state based on any calibrated EoS model is likely to be specially susceptible to experimental uncertainty in these specific data points.

Our uncertainty analysis also has implications for the determination of the run-to-detonation distance and time as it is typically obtained. These coordinates are used to characterize the sensitivity of a given material and also in certain instances, are used to to calibrate reactive flow models. In the present shot series, the run-to-detonation condition determination proceeds by determining the time and distance for the wave to reach 95% of its final velocity[15], as given from each individual curve fit to the shock tracker data. Given the series of fit variants already developed here, we can similarly generate uncertainty measures from the distribution of these two quantities (see Figure 10). The uncertainty measures are summarized in Table VIII and generally on the order of 0.4-2% of the baseline values. Therefore, though uncertainties in the shock velocity can be large for some range of time, the condition that the shock velocity reach a certain threshold value in the acceleration phase is relatively well-constrained. Again as in the shock velocity uncertainty, Gustavsen et al[19] estimated similar values, specifically 4.5% uncertainty in this metric due to wave tilt generated uncertainties in shock location. The present analysis adds to our understanding of how these experimentally derived detonation sensitivity measures generate inherent unaccounted for uncertainty, purely from known experimental errors. Whether these uncertainties (found to be at the level of tenths of mm or a few percent of baseline run distance values) have a significant effect on these calibrations is a subject that will be explored in the future.

TABLE VIII: The standard deviations for the run-to-detonation timing and distance.

Shot	P (GPa)	X_d (mm)	σ_{X_d} (mm)	σ_{X_d} (%)	T_d (μs)	σ_{T_d} (μs)	σ_{T_d} (%)
2s-1101	4.43	4.91	0.096	1.9	0.95	0.019	2.0
1s-1673	3.97	6.21	0.040	0.6	1.47	0.008	0.5
1s-1684	3.10	8.76	0.053	0.6	2.30	0.013	0.6
1s-1674	2.32	12.11	0.104	0.9	3.03	0.031	1.0

IV. DAVIS REACTANTS EOS

A. Model definition

The analytical (thermally-complete) EoS form employed in this work is the Davis reactants[8], a component of the Wescott-Stewart-Davis (WSD) reactive burn (RB) model[6] (and other variant models such as WSD-T[20] and AWSD[21]). Here we restate the main relations for this EoS which is of the Mie-Grüneisen form,

$$\begin{aligned} e(p,v) &= e^s(v) + \frac{v}{\Gamma(v)}(p - p^s(v)), \\ p(e,v) &= p^s(v) + \frac{\Gamma(v)}{v}(e - e^s(v)), \\ T(e,v) &= T^s(v)\left(\frac{1+\alpha_{str}}{C_{v,0}T^s(v)}(e - e^s(v)) + 1\right)^{\frac{1}{1+\alpha_{str}}}, \end{aligned} \tag{9}$$

where v is the specific volume, p is pressure, e is the internal energy and T is temperature. The Grüneisen gamma and isentrope reference functions are defined in a piecewise continuous form:

$$\Gamma(v) = \begin{cases} \Gamma_0 + Zy, v \le v_0 \\ \Gamma_0, v > v_0 \end{cases}, \tag{10}$$

$$p^s(v) = \begin{cases} \hat{p}\left[C\frac{(4By)^4}{4!} + \frac{y^2}{(1-y)^4} + \sum_{j=1}^{3}\frac{(4By)^j}{j!}\right], v \le v_0 \\ \hat{p}(\exp(4By) - 1), v > v_0 \end{cases} \tag{11}$$

$$e^s(v) = \begin{cases} \frac{1}{\rho_0}\int_0^y p^s(y')dy', v \le v_0 \\ \hat{p}(\exp(4By) - 1 - 4By)/(4B\rho_0), v > v_0 \end{cases}, \tag{12}$$

$$T^s(v) = \begin{cases} T_0 e^{-Zy}\left(\frac{v}{v_0}\right)^{-(\Gamma_0+Z)}, v \le v_0 \\ T_0(v/v_0)^{-\Gamma_0}, v > v_0 \end{cases} \tag{13}$$

where

$$y = 1 - v/v_0, \hat{p} = \rho_0 A^2/4B. \tag{14}$$

The parameters $A, B, C, \Gamma_0, Z, \alpha_{str}$ and $C_{v,0}$ define an instance of the Davis reactant EoS. Also, ρ_0, T_0, and $v_0 = 1/\rho_0$ are the ambient density, temperature, volume. This form has been proven to accomodate high explosive Hugoniot data for a number of explosives including PBX 9501[22]. Note that the thermal parameters $C_{v,0}$ and α_{str} define the Davis reactants form as a thermally complete EoS and have no direct incidence on the Hugoniot curve. Given the specific heat parameter, α_{str} can be obtained from thermal data if, for example, the von Neumann state temperature is known[8].

B. Calibration

The calibrated parameters were B and C while the remaining parameters were held fixed, i.e. A, Γ_0, $C_{v,0}$, α_{str} and Z, according to the following specifications. Parameter A is equivalent to the ambient sound speed and this was constrained to an experimental measurement of this quantity obtained for this work. The parameter Z was set to zero as it was not necessary to fit the data adequately. The parameter Γ_0 is determined from $\Gamma = \beta c_0^2/C_p$ (for thermodynamic

consistency as per Davis[8]) where β is the volumetric thermal expansion coefficient, C_p is the specific heat capacity at constant pressure and $c_0 = 1.99$ km/s is the measured ambient sound speed. From Dobratz and Crawford[18], we reasoned that LX-07 measurements of β and C_p could serve given its equivalent composition to PBX 9012 (i.e. $\beta = 189 \times 10^{-6}$/K and $C_p = 1210$ J/kg K). The specific heat at constant volume at ambient conditons, $C_{v,0}$, follows from the thermodynamic relation $C_p = C_v(1+\beta\Gamma T)^{-1}$, and is therefore 1170 J/kg K given our current estimates of Γ, β and C_v. Note that the remaining thermal parameter α_{str} is provisional, and we use a value such that at a shock velocity of 8.6 mm/μs this produces a von Neumann temperature of 1685 K which is reasonable.

To calibrate the relevant parameters, we used a composite error metric minimization approach, i.e. we numerically minimize

$$\mathscr{M} = \sqrt{\sum_i^N (U^i_{S,model} - U^i_{S,exp})^2 / N}, \tag{15}$$

where $U^i_{S,model}$ is the calculated model shock velocity, $U^i_{S,exp}$ is the experimental counterpart and N is the total number of experimental data points. This definition of $\mathscr{M}$ is equivalent to the root-mean-square (RMS) error measure between data and model. The optimized parameters are obtained via a gradient-based minimization approach[23] and appear in Table IX.

The comparison to the data is plotted in Figure 11 along with, for reference, relevant data and Davis reactants model for PBX 9501. The present model fits the data to a RMS shock velocity error of 288 m/s. This is comparable to the reported experimental scatter and to some of the uncertainty quantifications developed here. This figure also shows that the data for PBX 9501 is mostly constrained to lower shock velocities and is lower in number relative to PBX 9012. Nevertheless, the two computed EoS models are similar, at least in their overall trend. Also of note, the linear $U_S - u_p$ fit is shown to differ substantially from the calibrated Davis reactants form which has a better overall correspondence to the data specially for higher shock velocities (where the linear fit cannot accommodate the evident curvature in the data).

In addition to the calibration of the model from the base data set, we have also perturbed the source data for the EoS calibration in order to estimate the associated standard deviation of the optimized parameters (B and C). As in the shock tracker data case, we perturb the source $U_S - u_p$ data for the EoS calibration with Gaussian distributions with standard deviations consistent with the determined standard uncertainties for both U_S and u_p. The perturbed data is then fit using the same exact process as in the base model fit, producing a series of models and distributions of perturbed B and C. These distributions were then fit using Gaussian distributions themselves and the standard deviations of the parameters appear in Table IX. It is clear that in relative terms, the parameter B is more constrained by the data than C. Additionally, with the accumulated model variants, we can usefully estimate the uncertainty in any EoS-model-derived quantity. Given that shock or von Neumann pressure and temperature are commonly-used quantities to set reaction rate within reactive flow modeling, we choose to estimate these using a shock velocity of 8.6 mm/μs, as used previously in estimating the von Neumann temperature for the base model. As a result, we find that the von Neumann pressure and temperature mean and standard uncertainty are 49.7(1.4) GPa and 1679(52) K, respectively. Therefore, both quantities show a relative variation of 3% with respect to the mean which could have significant consequences for the uncertainty in reactive flow models that explicitly use these quantities to represent the strength of the post-shock reaction. This could be specially significant to those reaction rate models that use exponential functions to help set the reaction rate[21] and could amplify the uncertainty of any derived parameter set.

TABLE IX: The Davis reactants EoS form parameters. Note that only B and C were optimized. The standard deviation for each of these parameters were estimated from perturbing the source $U_S - u_p$ data via the determined standard uncertainties for both U_S and u_p.

Parameter	Value	Std. dev.	Unit
A	1.990000		mm/μs
B	3.261128	0.23	
C	2.071103	1.10	
Z	0.000000		
Γ_0	0.618500		
$C_{v,0}$	0.001170		kJ/g/K
α_{str}	0.623		
ρ_0	1.845000		g/cm^3

V. SUMMARY

Five experiments have been carried out to allow for calibration of the unreacted equation of state for the polymer-bonded explosive PBX 9012 and additionally, for forthcoming reaction rate calibration. The experimental data has been obtained in the form of particle velocity wave-profiles and shock tracker velocity data. These data have been used to present the relative shock sensitivity and the unreacted Hugoniot, both as a simple straight line approximation and the Davis reactants equation of state. The calibrated Davis reactants equation-of-state will form the basis of a complete reactive burn model whose reaction rate will be calibrated against the initiation wave profile data also produced here. Finally, a sensitivity analysis of the analytical fitting procedure to experimental uncertainty in the shock tracker was undertaken, producing novel measures of uncertainty in the reduced shock velocities and run-to-detonation coordinates.

VI. ACKNOWLEDGEMENTS

The authors would like to acknowledge Justin Jones and Andrew Houlton for their help in target preparation and firing and maintaining the Chamber 9 gas gun facility at LANL Technical Area 40. They would also like to thank

Kevin Vandersall for discussions on the estimated LX-07 Hugoniot and the assumptions therein. Thanks also go to Geoffrey Brown for his work on sound speed measurements, compositional analysis and compatibility testing of the various bonding agents. This work was supported by the US Department of Energy through the Los Alamos National Laboratory. Los Alamos National Laboratory is operated by Triad National Security, LLC, for the National Nuclear Security Administration of U.S. Department of Energy (Contract No. 89233218CNA000001).

The data that support the findings of this study are available from the corresponding author upon reasonable request.

VII. REFERENCES

[1]L. G. Green, R. J. Wasley, and P. E. Kramer. Shock initiation of LX-07-2 and LX-10-0. Technical Report UCRL-50851, California Univ., Livermore. Lawrence Radiation Lab., 1970.

[2]T. R. Gibbs and A. Popolato. *Explosive property data*. University of California Press, Berkeley, CA, 1980.

[3]R. L. Gustavsen, S. A. Sheffield, R. R. Alcon, and L. G. Hill. Shock initiation of new and aged PBX 9501. In *Proc. 12th Intl. Symp. on Detonation*, page 530, 2002.

[4]S. A. Sheffield, R. L. Gustavsen, and R. R. Alcon. In-situ magnetic gauging technique used at LANL-method and shock information obtained. In *AIP Conference Proceedings*, volume 505, pages 1043–1048. AIP, 2000.

[5]E. L. Lee and C. M. Tarver. Phenomenological model of shock initiation in heterogeneous explosives. *Phys. Fluids*, 23(12):2362–2372, 1980.

[6]B. L. Wescott, D. S. Stewart, and W. C. Davis. Equation of state and reaction rate for condensed-phase explosives. *J. Appl. Phys.*, 98(5):053514, 2005.

[7]J. Ramsey and A. Popolato. Analysis of shock wave and initiation data for solid explosives. In *Proc. 4th Intl. Symp. on Detonation*, pages 223–238, 1965.

[8]W. C. Davis. Complete equation of state for unreacted solid explosive. *Combust. Flame*, 120(3):399–403, 2000.

[9]Joint Committee for Guides in Metrology (JCGM). Evaluation of measurement data — guide to the expression of uncertainty in measurement. *Bureau International des Poids et Mesures (BIPM)*, 100, 2008.

[10]G. Brown. Personal communication.

[11]D. M. Dattelbaum, B. E. Clements, P. J. Rae, S. A. Sheffield, D. L. Robbins, E. B. Orler, M. Ahart, and R. Hemley. Pressure and strain rate effects in equation of state determination for polymers. Technical Report LA-UR-08-8030, Los Alamos National Laboratory, Los Alamos, NM USA, 2008.

[12]N. K. Bourne, J. C. F. Millett, G. T. Gray III, and P. Mort. On the strength behaviour of Kel-F-800 and Estane polymers. In *AIP Conference Proceedings*, volume 620, pages 653–656. AIP, 2002.

[13]L. M. Barker and R. E. Hollenbach. Shock-wave studies of PMMA, fused silica, and sapphire. *J. Appl. Phys.*, 41:4208–4226, 1970.

[14]K. Vandersall. Personal communication.

[15]L. G. Hill and R. L. Gustavsen. On the characterization and mechanisms of shock initiation in heterogeneous explosives. In *Proc. 12th Intl. Symp. on Detonation*, pages 975–987, 2002.

[16]J. Yao and D. S. Stewart. On the dynamics of multi-dimensional detonation. *J. Fluid Mech.*, 309:225–275, 1996.

[17]R.L. Gustavsen, S.A. Sheffield, and R. R. Alcon. Measurements of shock initiation in the tri-amino-tri-nitro-benzene based explosive PBX 9502: Wave forms from embedded gauges and comparison of four different material lots. *J. Appl. Phys.*, 99(114907), 2006.

[18]B. M. Dobratz and P. C. Crawford. LLNL explosives handbook, properties of chemical explosives and simulants. Technical Report Report UCRL-52997 Change 2, Lawrence Livermore National Laboratory, 1985.

[19]R. L. Gustavsen, R. J. Gehr, S. M. Bucholtz, R. R. Alcon, and B. D. Bartram. Shock initiation of the tri-amino-tri-nitro-benzene based explosive pbx 9502 cooled to- 55 c. *J. Appl. Phys.*, 112(7):074909, 2012.

[20]N. Desbiens, C. Matignon, and R. Sorin. Temperature-based model for condensed-phase explosive detonation. In *Journal of Physics: Conference Series*, volume 500, page 152004. IOP Publishing, 2014.

[21]T. D. Aslam. Shock temperature dependent rate law for plastic bonded explosives. *J. Appl. Phys.*, 123(14):145901, 2018.

[22]D. E. Lambert, D. S. Stewart, S. Yoo, and B. L. Wescott. Experimental validation of detonation shock dynamics in condensed explosives. *J. Fluid Mech.*, 546:227–253, 2006.

[23]J. A. Nelder and R. Mead. A simplex method for function minimization. *Comput. J.*, 7(4):308–313, 1965.

[24]J. J. Dick, A. R. Martinez, and R. S. Hixson. Plane impact response of PBX 9501 and its components below 2 GPa. Technical Report LA-13426-MS, Los Alamos National Laboratory, 1998.

(a)

(b)

FIG. 9: The evolution of the shock velocity uncertainty as a function of test time for all tests (both in a) absolute and b) relative terms). The solid circles on each curve represent the arrival times of the shock at the gauge locations (for cases used to generate shock Hugoniot data). The open circles represent the time of maximum acceleration for the baseline shock track fit used to generate the shock velocities in the Hugoniot data.

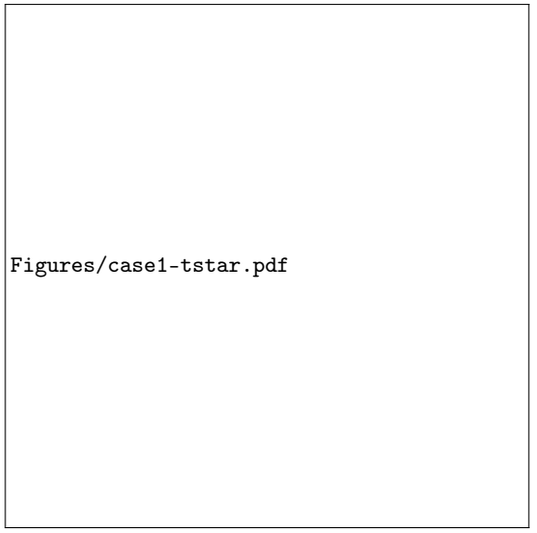

(a)

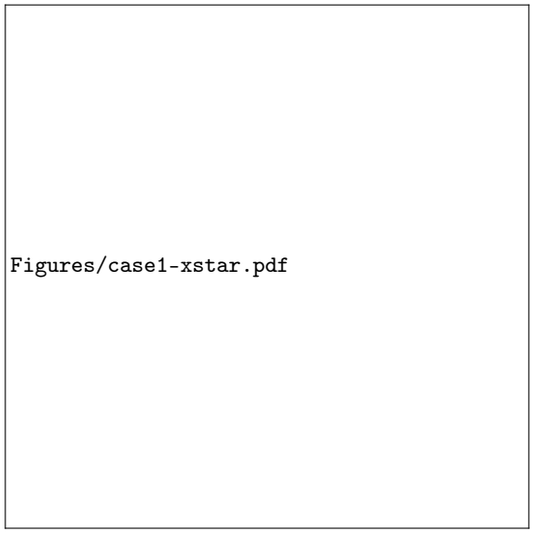

(b)

FIG. 10: Distribution of run-to-detonation time and distance for Shot 2s-1101. The uncertainty values for the time (a) and distance (b) derived from these are roughly 1.9% for both quantities in this case.

(a)

(b)

FIG. 11: Comparison of data and present modeling in both the U_S-u_p (a) and $P-v$ (b) planes, for PBX 9012 and additionally, for reference, equivalent information for PBX 9501 modeling[22] and experiment[24].

AIP Publishing

Journal of Applied Physics

ACCEPTED MANUSCRIPT

PLEASE CITE THIS ARTICLE AS DOI: 10.1063/1.5144686

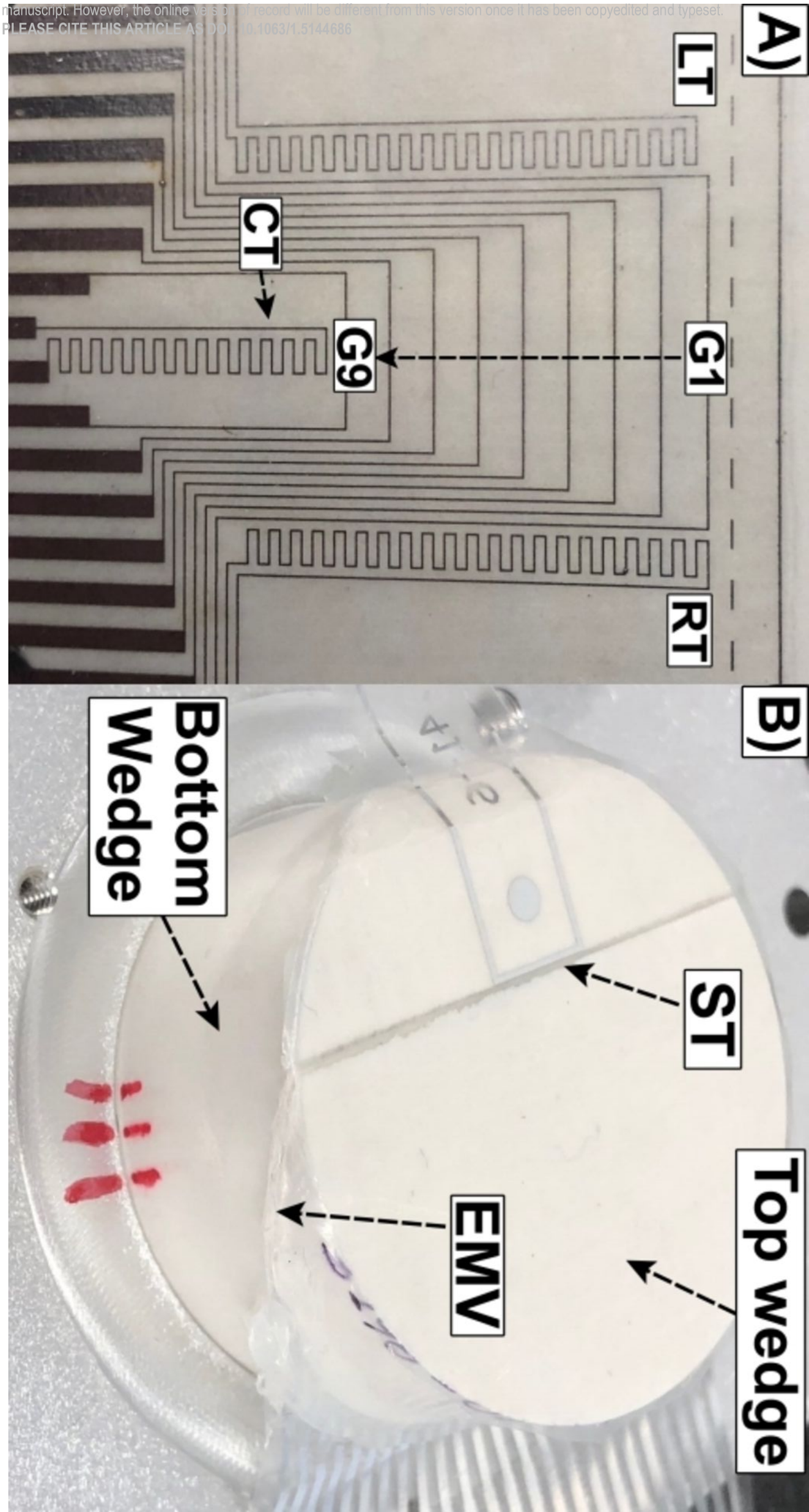

AIP Publishing

Journal of Applied Physics

PLEASE CITE THIS ARTICLE AS DOI: 10.1063/1.5144686

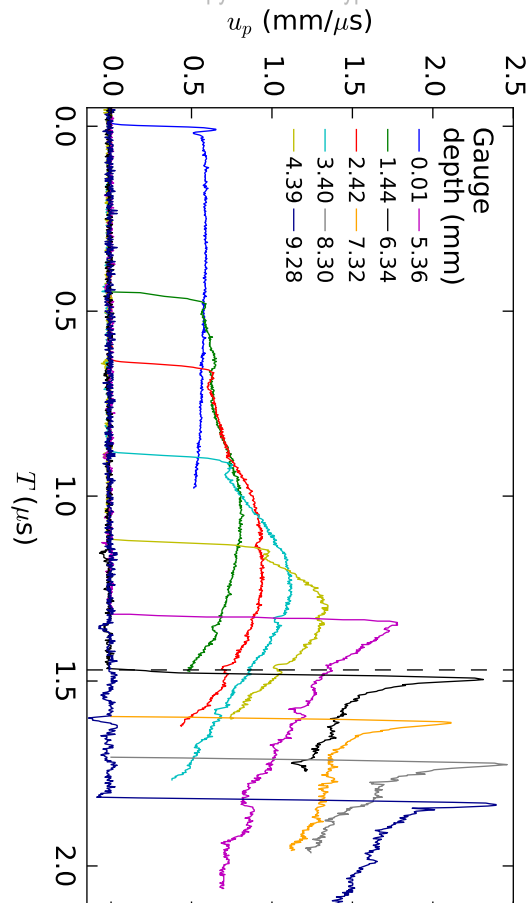

AIP Publishing

Journal of Applied Physics

PLEASE CITE THIS ARTICLE AS DOI: 10.1063/1.5144686

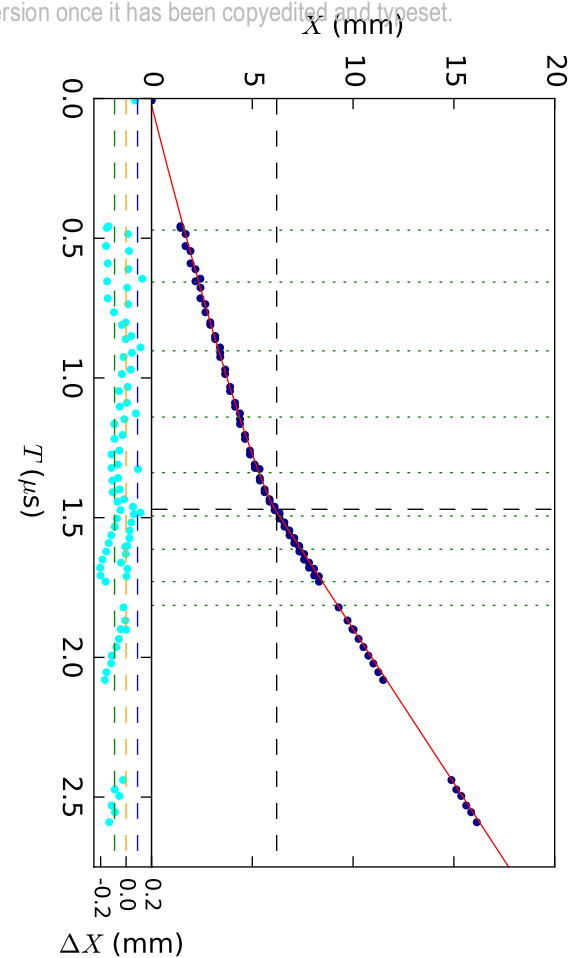

AIP Publishing

Journal of Applied Physics

PLEASE CITE THIS ARTICLE AS DOI: 10.1063/1.5144686

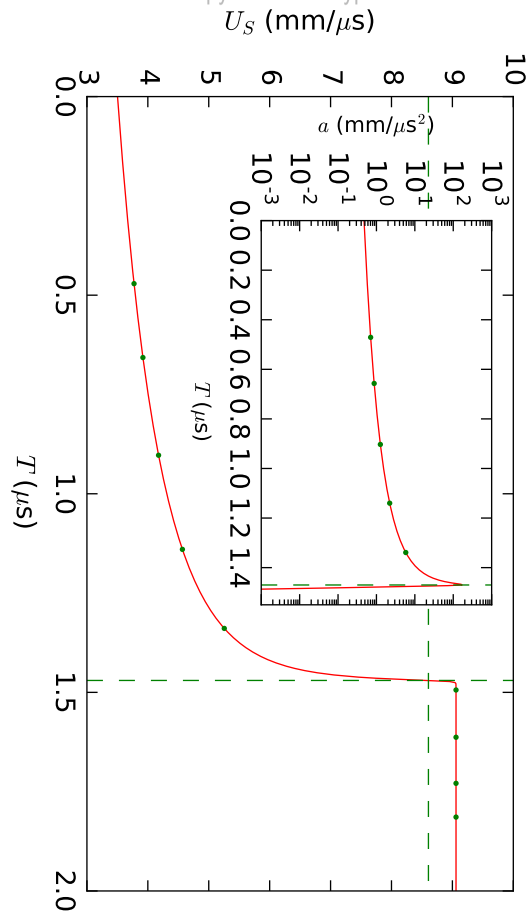

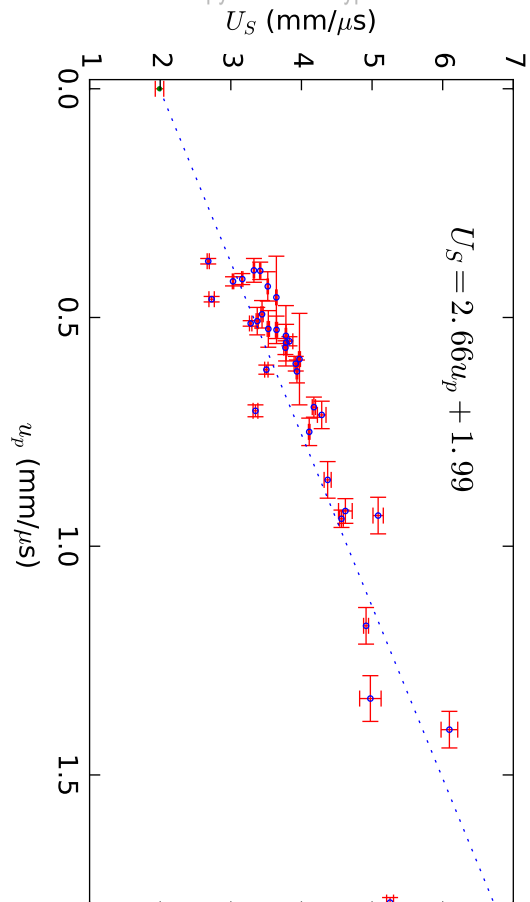

AIP Publishing

Journal of Applied Physics

ACCEPTED MANUSCRIPT

This is the author's peer reviewed, accepted manuscript. However, the online version of record will be different from this version once it has been copyedited and typeset.
PLEASE CITE THIS ARTICLE AS DOI: 10.1063/1.5144686

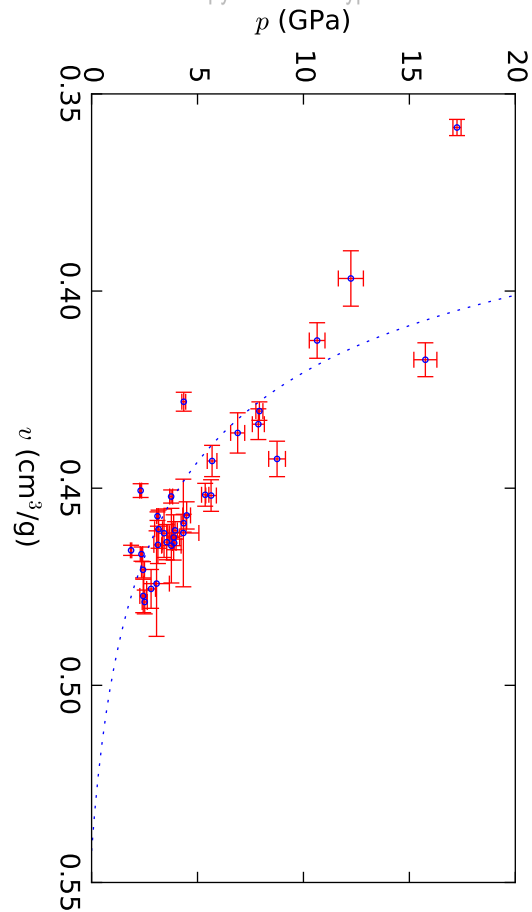

Journal of Applied Physics

PLEASE CITE THIS ARTICLE AS DOI: 10.1063/1.5144686

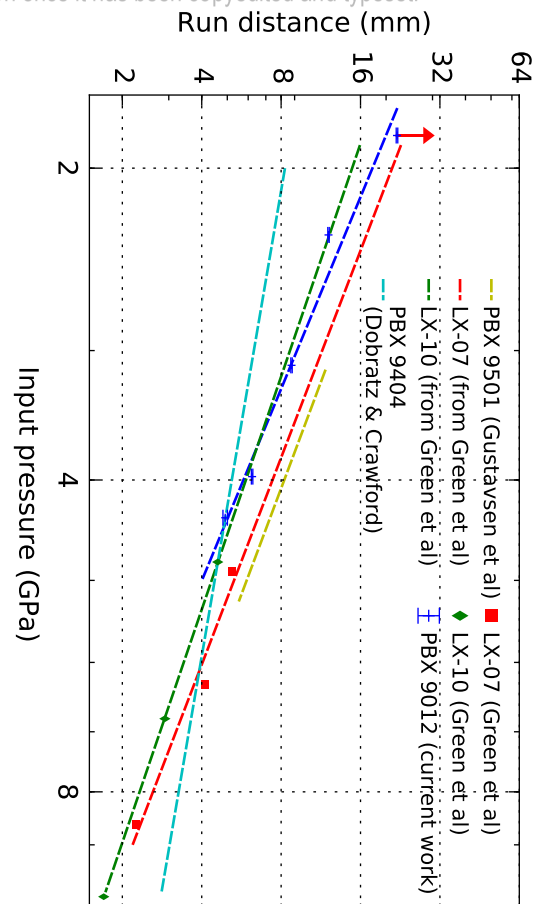

AIP Publishing

Journal of Applied Physics

ACCEPTED MANUSCRIPT

This is the author's peer reviewed, accepted manuscript. However, the online version of record will be different from this version once it has been copyedited and typeset.
PLEASE CITE THIS ARTICLE AS DOI: 10.1063/1.5144686

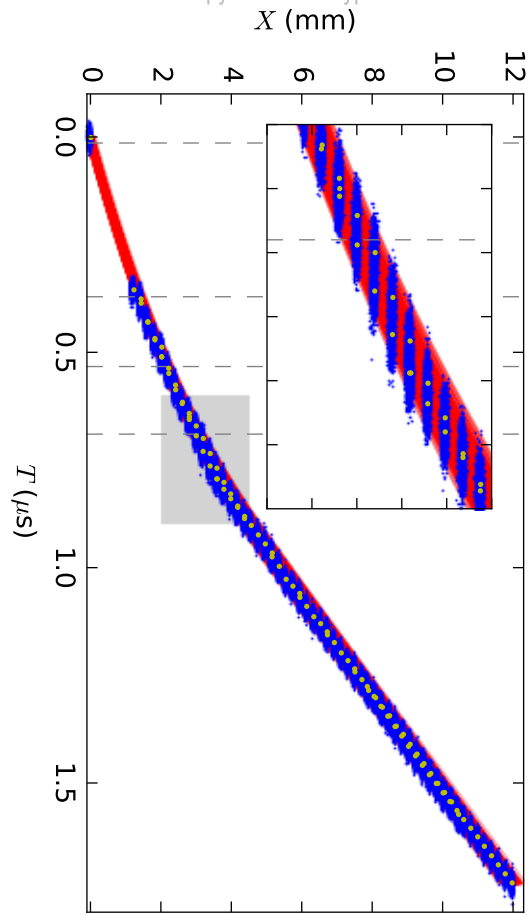

Journal of Applied Physics

PLEASE CITE THIS ARTICLE AS DOI: 10.1063/1.5144686

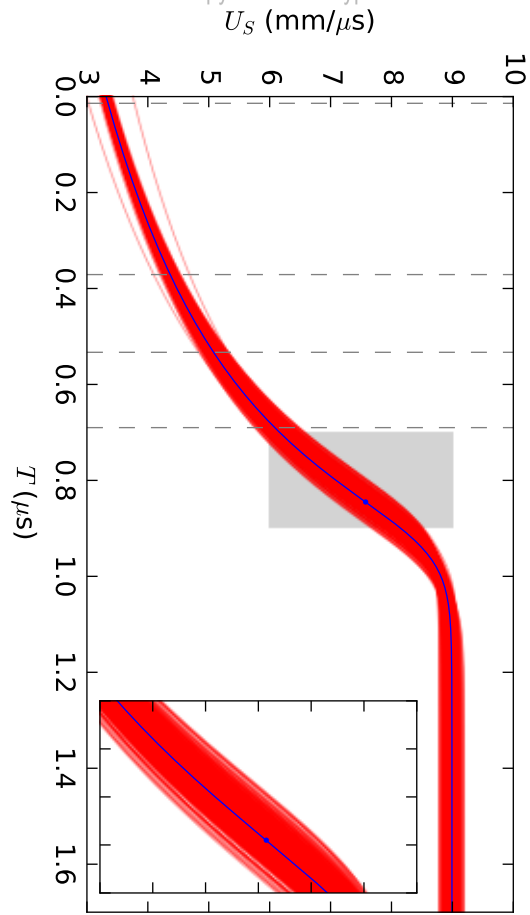

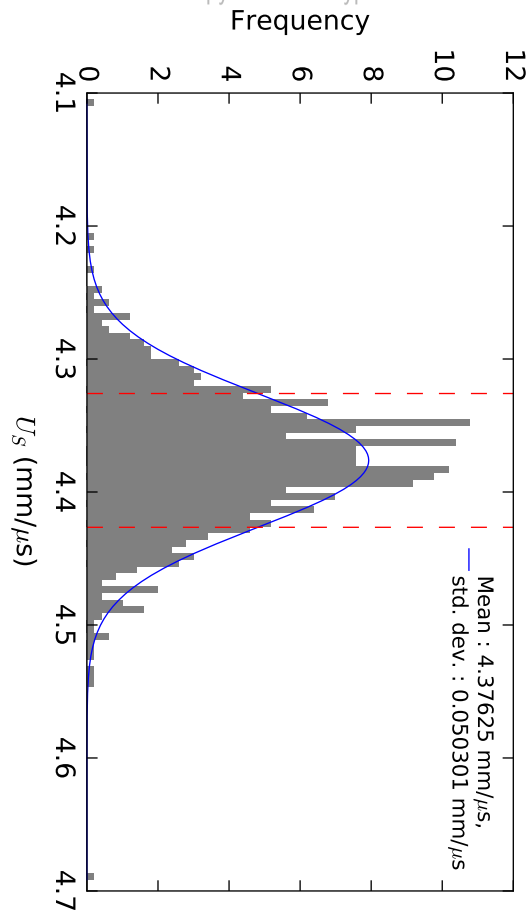

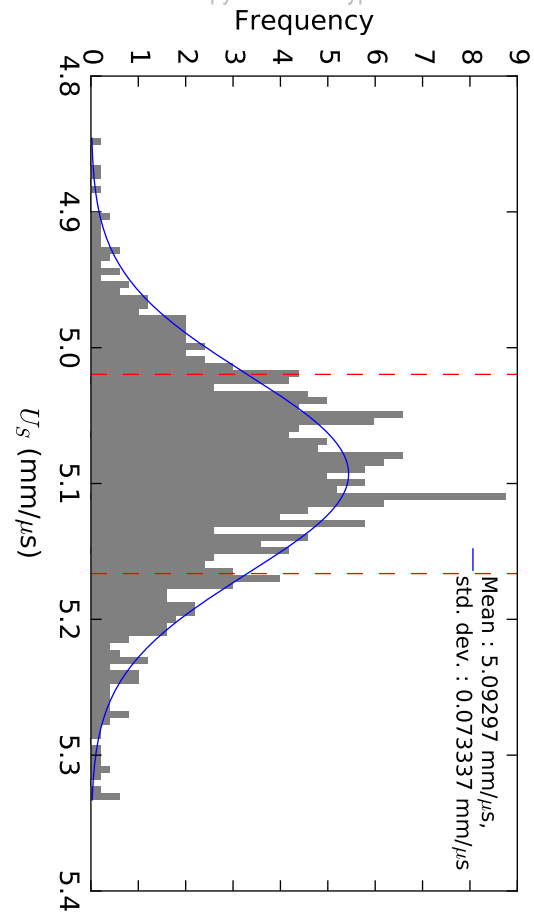

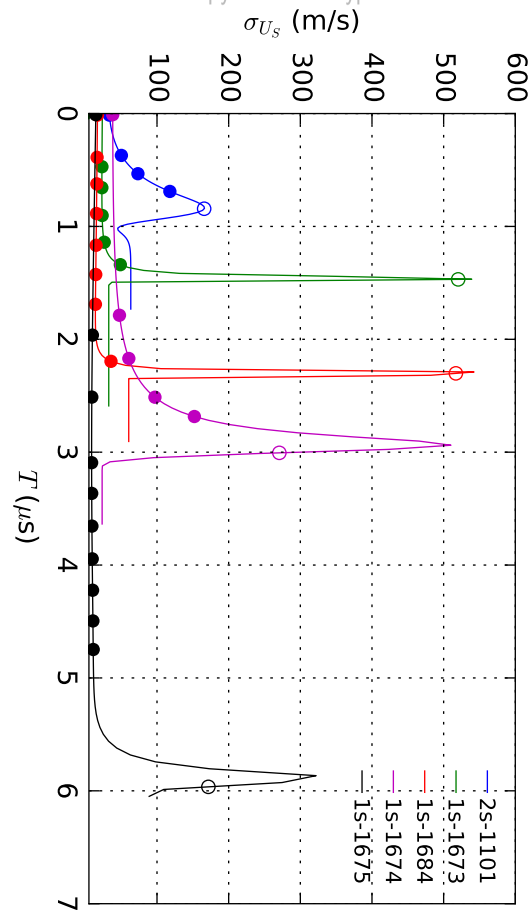

Journal of Applied Physics

PLEASE CITE THIS ARTICLE AS DOI: 10.1063/1.5144686

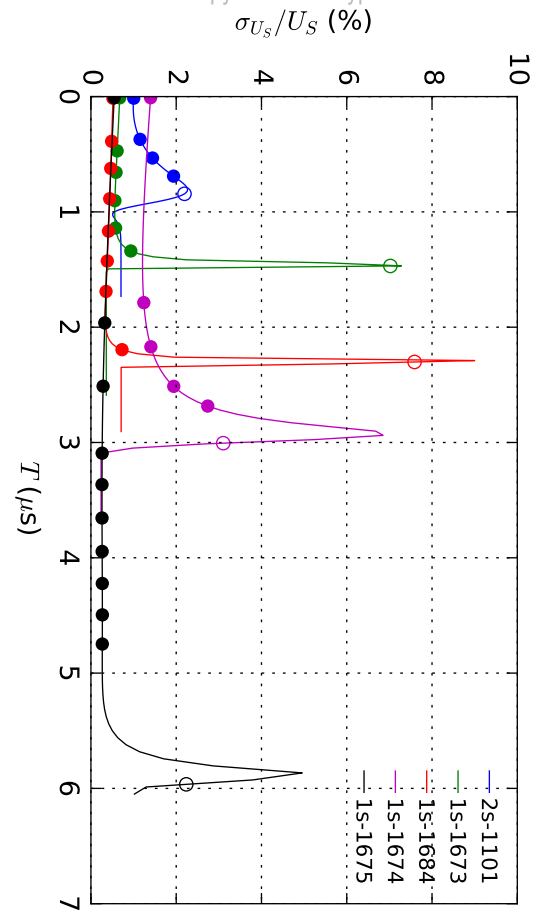

AIP Publishing

Journal of Applied Physics

ACCEPTED MANUSCRIPT

PLEASE CITE THIS ARTICLE AS DOI: 10.1063/1.5144686

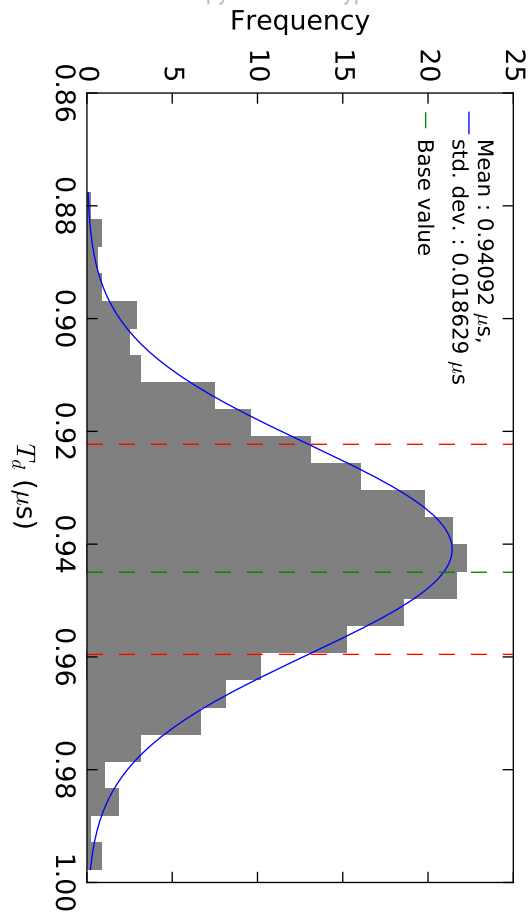

AIP Publishing

Journal of Applied Physics

ACCEPTED MANUSCRIPT

This is the author's peer reviewed, accepted manuscript. However, the online version of record will be different from this version once it has been copyedited and typeset.
PLEASE CITE THIS ARTICLE AS DOI: 10.1063/1.5144686

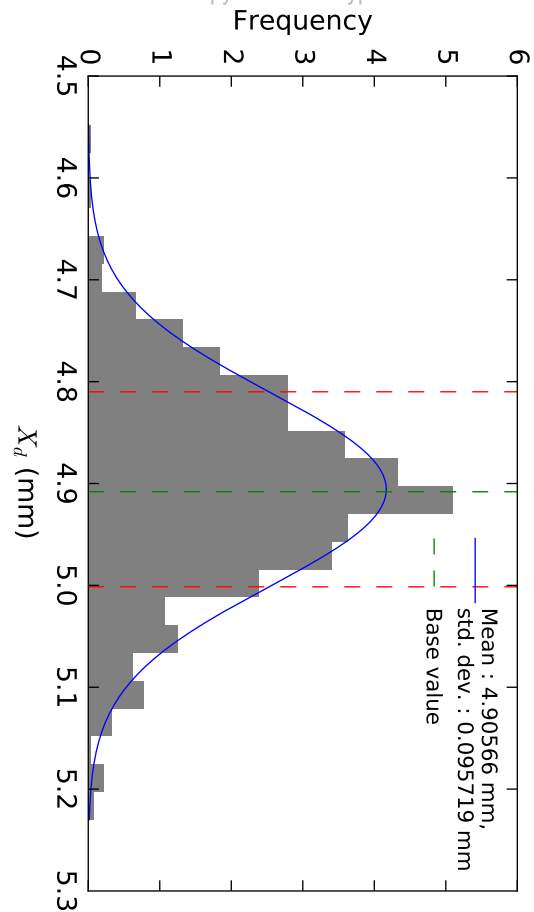

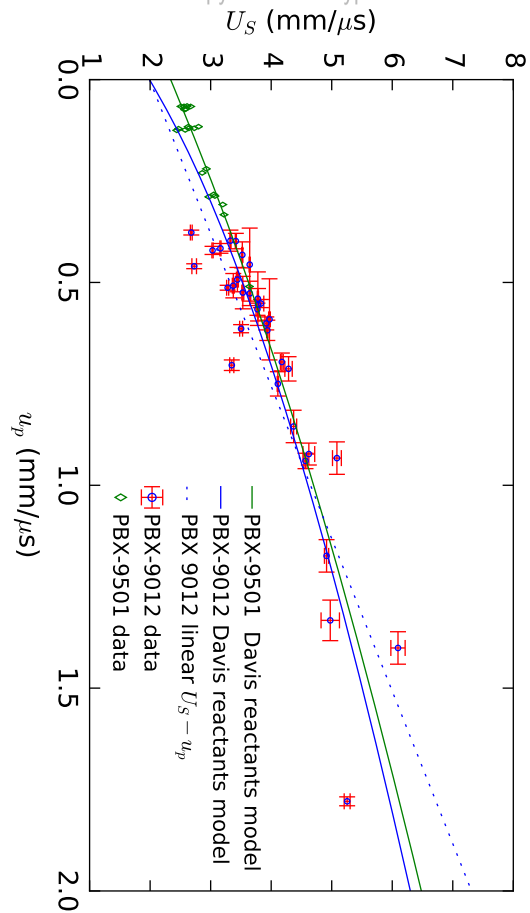

AIP Publishing

Journal of Applied Physics

ACCEPTED MANUSCRIPT

PLEASE CITE THIS ARTICLE AS DOI: 10.1063/1.5144686